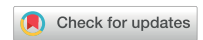
ENVIRONMENTAL RESEARCH

LETTERS



OPEN ACCESS

RECEIVED

10 June 2025

REVISED

7 September 2025

ACCEPTED FOR PUBLICATION 3 October 2025

PUBLISHED

21 November 2025

Original content from this work may be used under the terms of the Creative Commons Attribution 4.0 licence.

Any further distribution of this work must maintain attribution to the author(s) and the title of the work, journal citation and DOI.



LETTER

Exploring the optimal geometry of satellites Himawari-8/9 to monitor seasonal variation in vegetation dynamics across Southeast Asia

Misaki Hase^{1,2,*}, Kazuhito Ichii^{1,2,*}, Yuhei Yamamoto^{1,3}, Wei Li^{1,2}, Beichen Zhang^{1,2}, Wei Yang^{1,4}, Tomo'omi Kumagai^{5,6}, Yoshiaki Hata⁵, Naoya Takamura⁵, Chandra S Deshmukh⁷, Masahito Ueyama⁸, Hiroki Yoshioka⁹, and Tomoaki Miura^{10,11}

- ¹ Center for Environmental Remote Sensing (CEReS), Chiba University, Chiba, Japan
- ² Graduate School of Science and Engineering, Chiba University, Chiba, Japan
- ³ Institute for Advanced Academic Research, Chiba University, Chiba, Japan
- ⁴ Research Institute of Disaster Medicine, Chiba University, Chiba, Japan
- Graduate School of Agricultural and Life Sciences, The University of Tokyo, Tokyo, Japan
- Water Resources Research Center, University of Hawai'i at Mānoa, Honolulu, HI, United States of America
- Asia Pacific Resources International Limited, Pelalawan Regency, Indonesia
- ⁸ Graduate School of Agriculture, Osaka Metropolitan University, Sakai, Japan
- ⁹ Department of Information Science and Technology, Aichi Prefectural University, Aichi, Japan
- Department of Natural Resources and Environmental Management, University of Hawai'i at Mānoa, Honolulu, HI, United States of America
- Research Institute for Global Change, Japan Agency for Marine-Earth Science and Technology, Yokohama, Japan
- * Authors to whom any correspondence should be addressed.

E-mail: misakih1014@chiba-u.jp and ichii@chiba-u.jp

Keywords: Himawari-8/9, BRDF, Southeast Asia, geostationary satellite, vegetation monitoring, GPP, sun-target-sensor geometry Supplementary material for this article is available online

Abstract

Dense and widespread tropical rainforests across Southeast Asia are crucial for the global carbon cycle. A new generation geostationary satellite, Himawari-8/9, and onboard sensor, the Advanced Himawari Imager (AHI), enables hyper-temporal vegetation monitoring in this cloud-prone region. However, AHI's fixed viewing geometry varies spatially, making consistent vegetation monitoring challenging across a wide area at a seasonal scale. This study evaluated four different suntarget-sensor geometry conditions using two-band enhanced vegetation index (EVI2) to achieve near-uniform geometry and enhance the ability to monitor vegetation activities: (i) nadir condition, which used nadir viewing and solar geometry at local solar noon; (ii) local solar noon (LSN) condition, which used pixel-by-pixel fixed viewing and solar geometry at local solar noon; (iii) temporally-constant scattering angle (T-CSA) condition, which used pixel-by-pixel fixed viewing and solar geometry corresponding to the scattering angle which meets the criterion (Gao et al 2024 Remote Sens. Environ. 315 114407); and (iv) spatially-constant scattering angle (S-CSA) condition, which used pixel-by-pixel fixed viewing and solar geometry corresponding to a uniform scattering angle of 140°. Among these, the S-CSA condition most effectively mitigated angular artifacts. The derived EVI2 showed higher correlations with tower-based gross primary productivity (GPP), indicating it better captured seasonal variations in vegetation activity. It also demonstrated spatially consistent temporal variations, least affected by AHI's unique observation geometry. Applying a near-uniform sun-target-sensor geometry based on the S-CSA condition improves monitoring capability in Southeast Asia and enhances our understanding of vegetation dynamics.

1. Introduction

Southeast Asia is covered by dense and widespread tropical rainforests, which play a critical role in the global carbon cycle (Pan et al 2024). However, the terrestrial carbon cycle in this region remains uncertain due to the complex interplay of natural and anthropogenic factors (Bastos et al 2020). Among these,

the El Niño–Southern Oscillation strongly influences interannual variations in the region's carbon cycle (Kondo *et al* 2018). Furthermore, Southeast Asia has experienced one of the highest deforestation rates in the world in recent decades (Vancutsem *et al* 2021). These land-use changes are expected to significantly impact the regional carbon budget and accelerate climate change (Watson *et al* 2018). Therefore, understanding vegetation dynamics across Southeast Asia is essential.

Conventional polar-orbiting satellites can observe land surfaces approximately once per day and have been widely used for vegetation monitoring. For example, many studies have investigated the seasonal and interannual variations in vegetation activity across Southeast Asia using Moderate Resolution Imaging Spectroradiometer (MODIS) onboard Terra and Aqua (Huete *et al* 2008, Zhang *et al* 2016, Satriawan *et al* 2024). However, its low observation frequency prevented the acquisition of surface observations because of frequent and persistent cloud cover (Nagai *et al* 2014).

In recent years, various new-generation geostationary earth orbit (GEO) satellites have been launched, and their higher temporal resolution compared with that of polar-orbiting satellites has been utilized in applications such as fire detection (Hally et al 2019, Wiggins et al 2020) and the estimation of gross primary production (GPP) at the diurnal scale (Khan et al 2022, Jeong et al 2023, Li et al 2023). GEO satellites provide unprecedented opportunities for understanding vegetation dynamics in the Amazon (Hashimoto et al 2021, Zhang et al 2022) and Southeast Asia (Tian et al 2025). Particularly, the Himawari-8/9 GEO satellite equipped with the Advanced Himawari Imager (AHI) observes Asia and Oceania every 10 min. Tian et al (2025) investigated the seasonality of vegetation greenness in Southeast Asia by deriving normalized difference vegetation index (NDVI) from Himawari AHI surface reflectance data. However, this study did not focus on how accurately NDVI captures vegetation activity, highlighting the need for further investigation.

Despite high temporal frequency observations, the viewing geometry of GEO satellites makes spatial and temporal vegetation monitoring challenging. Unlike polar-orbiting satellites with a changing viewing geometry and fixed observation time, GEO satellites' viewing geometry remains fixed, whereas solar geometry changes diurnally and seasonally (Fensholt *et al* 2006). Variations in surface reflectance caused by the positions of the sun and sensor are known as the bidirectional reflectance distribution function (BRDF). These BRDF-induced reflectance changes can pose significant challenges for vegetation monitoring, as they may be misinterpreted as vegetation activity.

Various approaches have been explored to mitigate BRDF effects, including semi-empirical BRDF

models that adjust reflectance for specific observation geometries (Morton et al 2014). For polarorbiting satellites, nadir BRDF-adjusted reflectance (NBAR), which estimates reflectance at a nadir View Zenith Angle (VZA) at local solar noon, is commonly used (Schaaf et al 2002, Roy et al 2016). However, for the Himawari AHI, large VZAs over most parts of Southeast Asia (figure 1) make nadir normalization impractical due to angular extrapolation uncertainties (Zhang et al 2016). Additionally, semi-empirical models perform poorly under hotspot conditions when solar and viewing directions coincide (Schaaf et al 2002); using fixed solar geometry, such as local solar noon, may introduce noise due to hot-spot effects in some specific locations. Recently, Gao et al (2024) proposed the constant scattering angle (CSA) criterion in mid-latitude regions to mitigate the BRDF effects in GEO satellites. This approach selects observations such that the scattering angle remains constant, based on the assumption that surface reflectance primarily depends on the scattering angle rather than on the individual solar and viewing geometries. This method has been demonstrated to be effective in normalizing reflectance time-series and reducing directional influences in land surface monitoring. Since CSA was defined on a pixel-by-pixel basis, and spatial continuity was not considered. Moreover, its applicability to low-latitude regions remains unclear, where view azimuth angles around 90° are typically smaller than 110°–180° in mid-latitude regions, while VZAs remain similar at 0°-60°. This unique viewing geometry may cause biases such as longitude dependency in pixel-based approaches.

This study examined optimal sun-target-sensor geometry across Southeast Asia to achieve near-uniform geometry and enhance the ability to monitor vegetation activities, including GPP, at seasonal scale. We evaluated four different geometry conditions using the two-band enhanced vegetation index (EVI2), based on comparison with flux tower-based GPP at the site scale and spatial patterns of EVI2 at sub-continental scales. Among them, the spatially-CSA (S-CSA) condition, proposed in this study, most effectively mitigated BRDF effects. Inspired by the CSA criterion (Gao *et al* 2024), this approach used a uniform scattering angle across Southeast Asia, rather than a pixel-based approach, to enable direct pixel-to-pixel comparisons.

2. Materials and methods

2.1. Study area and flux tower measurement sites

The study area consists of the Indochina Peninsula, Malay Peninsula, Borneo, Sumatra, and surrounding islands with six eddy-covariance tower observation sites registered in AsiaFlux (www.asiaflux.net) (figure 1 and table S1). The landcover predominantly comprises evergreen tropical forests and

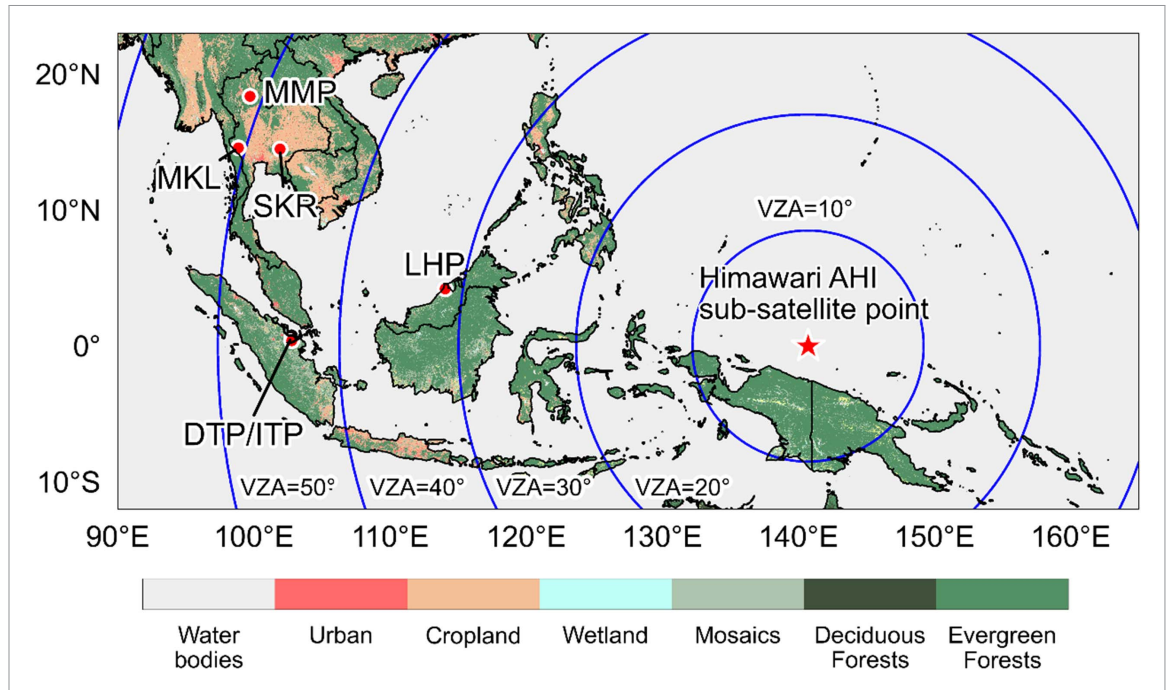


Figure 1. Study region and location of flux tower sites used in this study. The landcover is based on copernicus global land service: land cover 100 m: collection 3 product (Buchhorn *et al* 2020). The Himawari AHI sub-satellite point is shown as a star. Himawari AHI 10°, 20°, 30°, 40°, and 50° view zenith angles (VZAs) are indicated with blue circles.

croplands. Among the six sites, Lambir Hills National Park (LHP) (Takamura *et al* 2023), degraded tropical peatland (DTP), and intact tropical peatland (ITP) (Deshmukh *et al* 2021) are located in moist tropical forest regions characterized by abundant rainfall throughout the year and no distinct wet or dry seasons. The other three sites, the Mae Klong (MKL), Sakaerat (SKR) (Ishida *et al* 2010), and Mae Moh plantation (MMP) (Yoshifuji *et al* 2006), are located in dry tropical regions characterized by distinctive wet and dry seasons.

2.2. Eddy-covariance data

We estimated GPP data by flux-partitioning, using the observed net ecosystem exchange (NEE) for the six sites (Reichstein *et al* 2005). The GPP datasets for the LHP and MMP sites were based on the JapanFlux2024 dataset (Ueyama *et al* 2025). For the DTP and ITP sites, we used the GPP dataset published in Deshmukh *et al* (2021). For the MKL and SKR sites, NEE data provided in the AsiaFlux database were converted to GPP based on Ichii *et al* (2017) and Ueyama *et al* (2012). Using these post-processed GPP data, we created a 16-day accumulation dataset.

2.3. Himawari AHI land surface reflectance data and their BRDF parameter retrieval

We used Himawari AHI surface reflectance data from red (0.64 μ m) (RED) and near-infrared (0.86 μ m) (NIR) bands (Li *et al* 2025, Zhang *et al* 2025. The data were geometrically corrected and re-gridded from Himawari standard data (Takenaka *et al* 2020, Yamamoto *et al* 2020). The temporal and spatial resolutions were 10 min and 0.01°, respectively.

The analysis covered 02:00–08:00 UTC (9:00–15:00 Indonesia Western Standard Time for the DTP, ITP, MKL, SKR, and MMP sites and 10:00–16:00 Indonesia Central Standard Time for the LHP site) from 1 January 2018 to 31 December 2019. For data screening, we applied cloud filtering based on Yamamoto *et al* (2018) and excluded cases with aerosol optical thickness at 500 nm greater than 0.6.

We further applied a kernel-driven semiempirical BRDF model, the Ross-Thick (RTK) and Li-Sparse-Reciprocal (LSR) kernel models (Li and Strahler 1992), to estimate reflectance under specific geometry conditions. This model is widely employed for BRDF parameter estimation and correction for both polar-orbiting (Lucht *et al* 2000, Schaaf *et al* 2002) and GEO satellites (Zhang *et al* 2021, Li *et al* 2025). The estimated reflectance is expressed as:

$$\rho_{(\theta_{s},\theta_{v},\varphi_{s}-\varphi_{v})} = f iso + f vol \cdot K vol_{(\theta_{s},\theta_{v},\varphi_{s}-\varphi_{v})}$$

$$+ f g eo \cdot K g eo_{(\theta_{s},\theta_{v},\varphi_{s}-\varphi_{v})}$$
 (1)

where ρ is the reflectance, θ_s and φ_s are the solar angles, θ_v and φ_v are the view angles, Kvol and Kgeo are the RTK kernel for the volume kernel, and the LSR kernel for the geometric kernel, and fiso, fvol, and fgeo are the model parameters. BRDF parameters were obtained via multiple linear regression on a pixel basis using the reflectance after data screening and kernels with a 15 d rolling window. The regression was applied only when at least ten valid observations were available in seven days before and after the target date, with at least three in both the morning and afternoon.

2.4. Analysis

Since we assumed that the choice of sun-target-sensor geometry is essential to monitor seasonal variations in vegetation activities using the Himawari AHI, four different geometry conditions were tested: (i) nadir, (ii) local solar noon (LSN), (iii) temporally-constant scattering angle (T-CSA), and (iv) spatially-constant scattering angle (S-CSA) conditions.

- i. Nadir condition (figure S1 (a)): Nadir viewing (i.e. $\theta_{\rm v}=0^{\circ}$) and solar geometry at local solar noon (Camacho-de Coca *et al* 2004) were used. This condition is adopted in MODIS and VIIRS NBAR products (MCD43, VNP43) (Schaaf *et al* 2002, Liu *et al* 2017).
- ii. LSN condition (figure S1(b)): Pixel-by-pixel fixed viewing and solar geometry at local solar noon were used.
- iii. T-CSA condition (figure S1(c)): Pixel-by-pixel fixed viewing and solar geometry corresponding to the scattering angle closest to CSA, as defined by Gao *et al* (2024), were used. The scattering angle (θ), the angle between the incident solar vector (from the sun to object) and the viewing vector (from object to sensor), is defined as follows (Iqbal 1983):

$$\cos\theta = -\cos\theta_{\rm s}\cos\theta_{\rm v} - \cos\left(\varphi_{\rm s} - \varphi_{\rm v}\right)\sin\theta_{\rm s}\sin\theta_{\rm v} \ . \eqno(2)$$

The backscattering condition (i.e. when the sensor views the surface near the solar backscattering direction, thereby minimizing shadowing and enhancing canopy reflectance) occurs at larger scattering angles (figure S2), and hot-spot conditions ($\theta > 175^{\circ}$) can lead to significantly increased reflectance (Vermote and Roy 2002). CSA was determined for each pixel based on scattering angles at the summer and winter solstices (Gao *et al* 2024). In the study region, the determined CSA ranged from 152° to 157°.

iv. S-CSA condition (figure S1(d)): Pixel-by-pixel fixed viewing and solar geometry corresponding to the scattering angle closest to 140° over the entire region were used. In the study region, the common candidate range of scattering angles across the domain was 132°–152° since the scattering angle takes 132°–156° at the pixel nadir of the sub-satellite point and 95°–152° at the farthest pixel (23° N, 90° E) throughout the year. Among these values, 140° was selected as CSA to avoid backscattering conditions and to prevent the use of extreme angles (e.g. 132° or 152°), which could bias observation geometry toward morning or evening.

To express seasonal vegetation dynamics, we applied mean compositing (MC) to generate a 16-day composite EVI2 from surface reflectance (Jiang et al.)

2008). EVI2 is known to be more effective in highly dense vegetation and less affected by clouds or aerosol contamination than NDVI (Huete *et al* 2002). The MC algorithm is the most effective in reducing the noise induced by residual BRDF and atmospheric effects (Vancutsem *et al* 2007).

We evaluated the effectiveness of each geometry condition at both site and sub-continental scales. First, we analyzed time-series of scattering angles and corresponding solar zenith angles (SZAs) at each site to assess geometric variation among the four geometry conditions. Then, we evaluated the reliability of EVI2 by comparing a 16-day composite EVI2 with tower-based GPP. All variables were extracted from pixels corresponding to each site location. Note that both EVI2 and GPP reflect vegetation activity but are sensitive to different aspects. EVI2 better represents canopy structure (Jiang et al 2008), while GPP further reflects photosynthetic activity and is more sensitive to environmental stress. Pearson's correlation coefficient was used to quantify their relationship. At MKL, SKR, and MMP, where GPP data were unavailable for 2018-2019, EVI2 and GPP were averaged across available years, assuming no landcover changes.

On a sub-continental scale, we investigated the spatial uniformity of the seasonal variation range and magnitude of EVI2. The variation range was assessed using amplitude, defined as the difference between annual maximum and minimum EVI2, averaged over 2018–2019. To evaluate EVI2 magnitude, we generated longitudinal profiles of annual mean EVI2 for evergreen forests within the equatorial region (i.e. $\pm 2.5^{\circ}$ N/S). Evergreen forests are predominantly distributed in this region (figure 1) and exhibit some of the smallest seasonal variations worldwide. Therefore, we assumed that EVI2 values should remain relatively constant across longitudes at the equator.

3. Results

3.1. Site-level analysis

Time-series of the scattering angle and SZA differed substantially across the four geometry conditions (figure 2). The scattering angle under the Nadir condition showed wide variation ranges, from approximately 140°-180°. By contrast, under the LSN condition, the scattering angle exhibited moderate variations, with a seasonal change of approximately 10° within 125°-150° across all sites. As defined, the T-CSA and S-CSA conditions maintained nearly constant throughout the year, while the T-CSA condition showed slight differences depending on the sites. Regarding SZA, both Nadir and LSN conditions represented SZA at local solar noon. Conversely, the T-CSA condition consistently yielded larger SZA than the LSN condition throughout the year, especially during day of year (DOY) 130-200, when it deviated significantly from local solar noon. The S-CSA

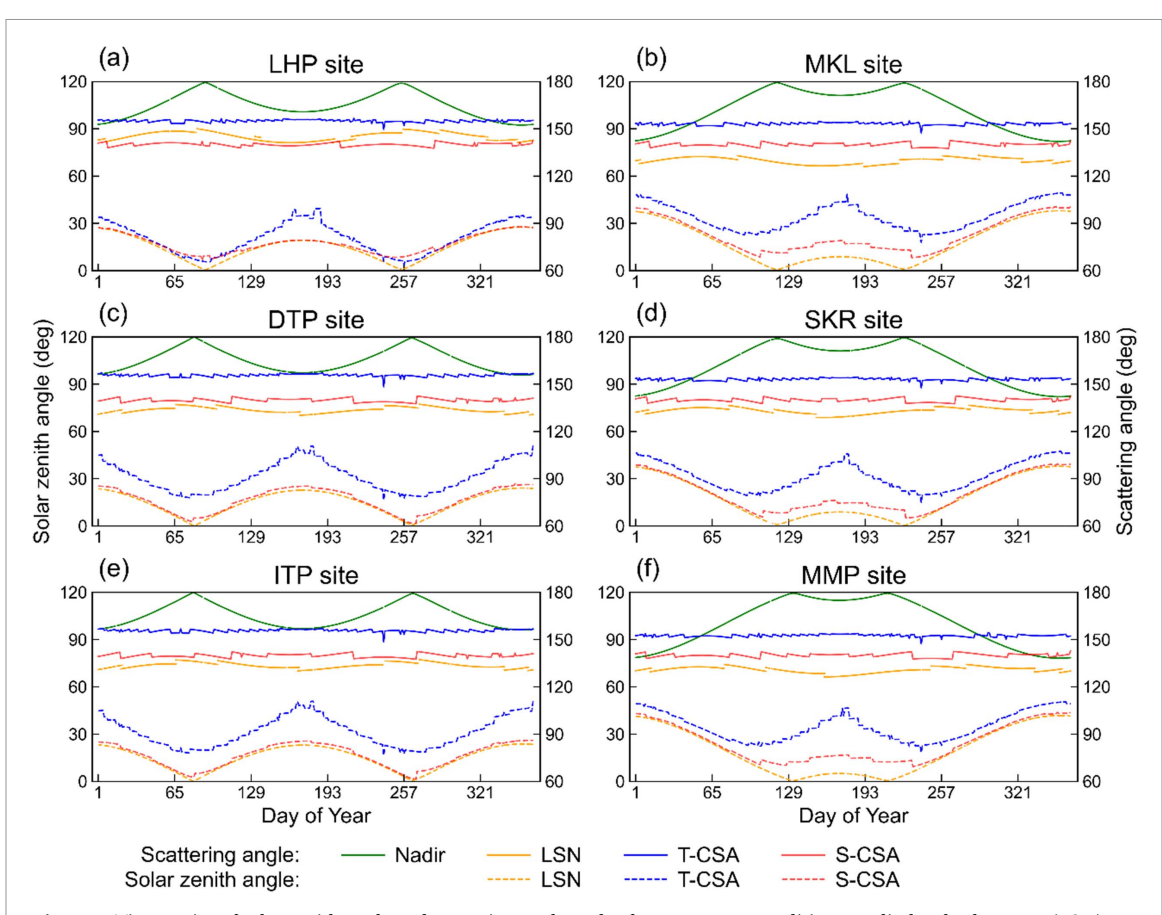


Figure 2. Time-series of solar zenith angle and scattering angle under four geometry conditions: nadir, local solar noon (LSN), temporally-constant scattering angle (T-CSA), and spatially-constant scattering angle (S-CSA) conditions at the (a) Lambir Hills National Park (LHP), (b) Mae Klong (MKL), (c) degraded tropical peatland (DTP), (d) Sakaerat (SKR), (e) intact tropical peatland (ITP), and (f) Mae Moh plantation (MMP) sites.

condition exhibited SZA smaller than that under the T-CSA condition and remained closer to the LSN condition.

Among the four geometry conditions, EVI2 under the LSN and S-CSA conditions showed the highest correlation with GPP, followed by the T-CSA condition, while the Nadir condition had the lowest correlation (figure 3). For the LSN and S-CSA conditions, significant correlations were found in five out of the six sites. At the LHP, DTP, and ITP sites, EVI2 under both geometry conditions exhibited lower correlation coefficients than at the MKL, SKR, and MMP sites. However, it displayed stable and small seasonal variations, characteristic of evergreen forests near the equator. Particularly at the DTP and ITP sites, EVI2 showed a similar variation to GPP, with a peak around February, followed by a slight decrease. For the T-CSA and Nadir conditions, significant correlations were observed in only four sites and one site, respectively. EVI2 under the Nadir condition fluctuated substantially regardless of the vegetation type. For example, EVI2 varied by more than 0.6 over 16 d at the DTP and ITP sites, even in evergreen forests. For the T-CSA condition, EVI2 showed noticeable increases around DOY 130-200 at all sites, differing from EVI2 timeseries under other conditions as well as tower-based GPP.

3.2. Regional scale analysis

The S-CSA condition produced the most spatially consistent distribution of seasonal EVI2 amplitude (figure 4(d)). The Nadir condition exhibited large amplitudes across the entire region, including evergreen forests (figures 1 and 4(a)). The LSN condition better reflected landcover compared with that of the Nadir condition (figures 1 and 4(b)). For example, evergreen forests showed smaller amplitudes (<0.10), whereas croplands exhibited larger ones (>0.25). However, the LSN condition yielded larger amplitudes (>0.15) near the sub-satellite point (e.g. New Guinea) than in other evergreen forests at similar latitudes. The T-CSA condition demonstrated a notable longitude dependency (figure 4(c)). Among equatorial evergreen forests (e.g. Sumatra Island, Borneo Island, and New Guinea), the amplitude increased from ~ 0.05 to ~ 0.20 as the distance from the subsatellite point increased. Finally, the S-CSA condition exhibited clear correspondence with landcover, without the regional bias seen in the LSN condition and the longitude dependency of the T-CSA condition (figure 4(d)).

The longitudinal profiles of the annual mean EVI2 showed that the S-CSA condition remained nearly uniform across all longitudes (figure 4(e)). Under the LSN condition, EVI2 increased eastward

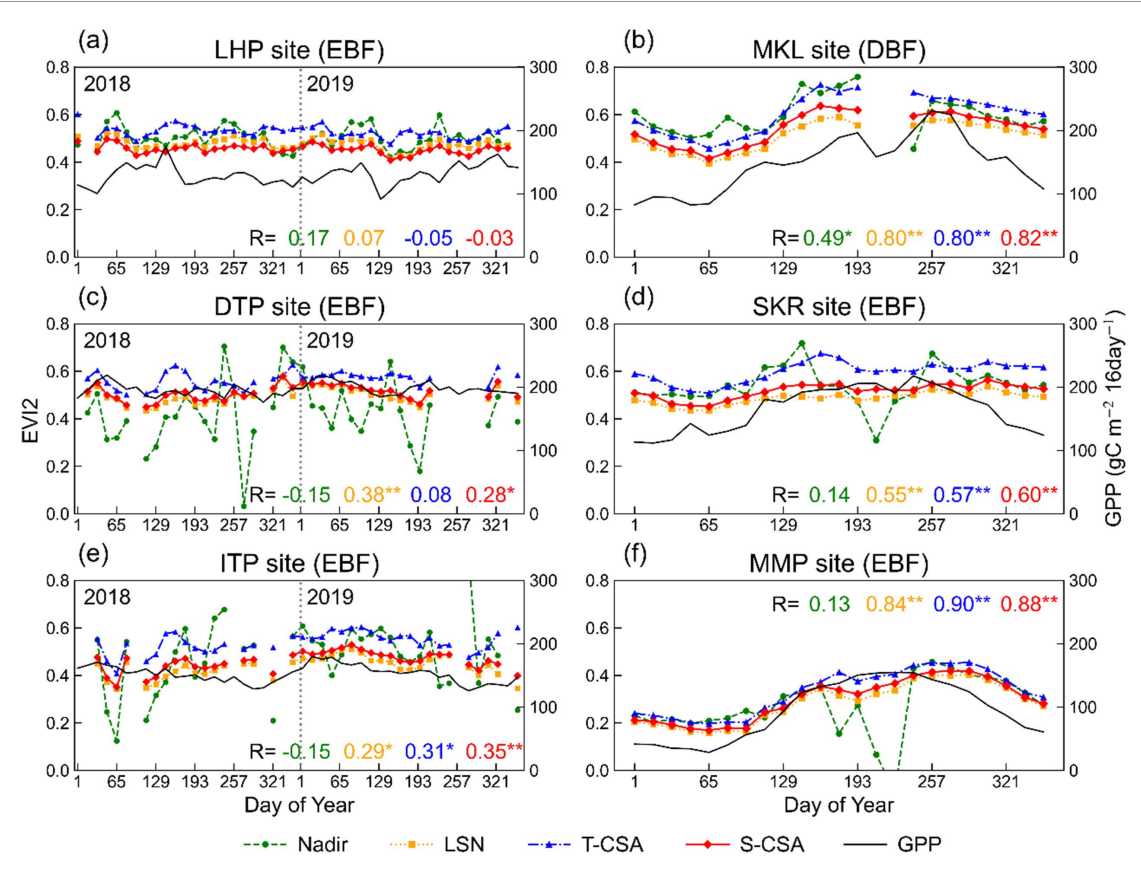


Figure 3. Time-series of 16-day two-band enhanced vegetation index (EVI2) derived from the four geometry conditions and gross primary productivity (GPP) (black line) at the (a) Lambir Hills National Park (LHP), (b) Mae Klong (MKL), (c) degraded tropical peatland (DTP), (d) Sakaerat (SKR), (e) intact tropical peatland (ITP), and (f) Mae Moh plantation (MMP) sites. The conditions include the Nadir (green dashed line), local solar noon (LSN) (orange dashed line), temporally-constant scattering angle (T-CSA) (blue dashed line), and spatially-constant scattering angle (S-CSA) conditions (red line). EBF and DBF indicate evergreen broadleaf forest and deciduous broadleaf forest, respectively. At the MKL, SKR, and MMP sites, 16-day EVI2 and GPP were averaged for available years. R values indicate Pearson's correlation coefficients between EVI2 and GPP, with * and ** denoting statistical significance at p < 0.1 and p < 0.01, respectively.

(0.011/deg, p < 0.001), with a sharp increase from approximately 0.51 at $130^{\circ}-135^{\circ}$ E to 0.56 at $135^{\circ}-140^{\circ}$ E, near the sub-satellite point. By contrast, the T-CSA condition displayed a westward increasing trend in EVI2 (0.008/deg, p < 0.0001). In the Nadir condition, no explicit longitudinal dependency was evident, but unlike the other conditions, the variance in EVI2 between pixels increased substantially in the western region.

4. Discussion

Examining EVI2 variations under the four different geometry conditions at site and sub-continental scales, our study demonstrated that the S-CSA condition minimizes BRDF effects and spatial discontinuities. Under the Nadir condition, the extrapolation of pixel-by-pixel fixed viewing geometry to the nadir resulted in large fluctuations in derived reflectance (figure S3) (Gao et al 2001, Zhang et al 2016a) and thus EVI2 (figures 3 and 4(a)). The uncertainty increased with distance from the Himawari AHI

sub-satellite point, as extrapolated angles become larger (figure 4(e)). The LSN condition, which selects the smallest SZA of the day, mitigated solar angle effects and enhanced the correlation between EVI2 and tower-based GPP (figure 3). However, near the subsatellite point, both the magnitude and amplitude of EVI2 sharply increased (figures 4(b) and (e)) due to hot-spot conditions ($\theta > 175^{\circ}$) occurring twice a year around local solar noon (figure S4(a)). This introduces regional biases because, unlike general BRDF effects that produce gradual geometry-dependent variations in reflectance, hot-spot effects produce anomalously high reflectance. Specifically, at a pixel in this region, RED and NIR increased by ~20% and \sim 35%, respectively, under hot-spot conditions, causing EVI2 rises of approximately 40% (figures S4(b) and (c)). Similar hot-spot artifacts were reported for GOES-16 ABI reflectance (Li et al 2021) and appear in other indices such as NDVI and NIRv. This issue is particularly critical for GEO satellites, which continuously observe the same region; thus, hotspot geometries can systematically recur around local solar noon in specific locations, amplifying regional

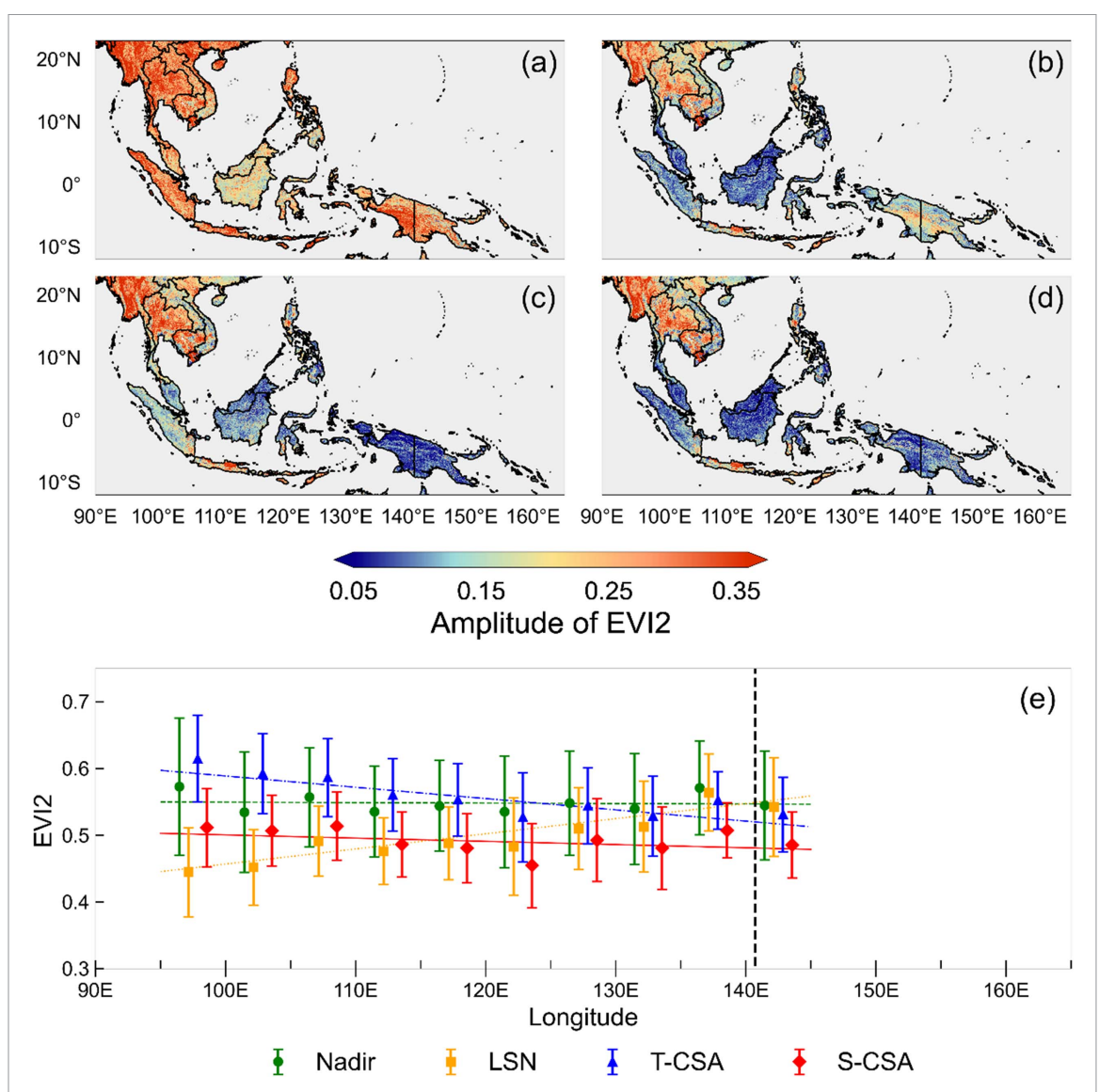


Figure 4. (a)–(d) Amplitude of 16-day two-band enhanced vegetation index (EVI2) derived from the (a) Nadir, (b) local solar noon (LSN), (c) temporally-constant scattering angle (T-CSA), and (d) spatially-constant scattering angle (S-CSA) conditions. Amplitude is defined as the mean difference between the annual maximum and minimum EVI2 in 2018 and 2019. (e) Annual mean EVI2 profiles for every 5° of longitude in the equatorial region (i.e. $\pm 2.5^{\circ}$ N/S). Only EVI2 from areas where land pixels account for at least 5% are shown. Error bars represent the standard deviation ($\pm 1~\sigma$). The dashed line indicates the longitude of the Himawari AHI sub-satellite point.

biases. Our results further support the importance of avoiding hot-spot conditions for accurate vegetation monitoring.

Larger SZAs selected under the T-CSA condition, compared to those at local solar noon, lead to solar angle effects that intensify with increasing distance from the sub-satellite point (figures 2, 4(c) and (e)). Across Southeast Asia, the selected CSA exceeded 150°, indicating backscattering conditions that increase reflectance. Since most of the region lies west of the Himawari AHI, this backscattering primarily occurs in the morning (figure S2(a)). The particularly large SZA selected for DOY 130–200 thus corresponds to early morning observations, further elevating reflectance (figure S3). This affects not only EVI2 (figure 3) but also other vegetation indices. Additionally, the impact of solar angle effects

varies by the distance from the sub-satellite point. For instance, although the DTP, ITP, and LHP sites are at similar latitudes, the DTP and ITP sites, located farther west, showed larger annual SZA variations (figures 2(a), (c) and (e)). Correspondingly, the EVI2 variation ranges exceeded 0.10, while \sim 0.07 at the LHP site (figures 3(a), (c) and (e)). These findings suggest that increased distance introduces longitudedependent variations in EVI2, also apparent in the spatial patterns (figures 4(c) and (e)). However, such a trend was not observed in EVI2 profiles derived from MODIS NBAR (0.000/deg, p = 0.85) (figure S5). This indicates that the observed increase is likely attributable to solar angle effects rather than actual vegetation changes, emphasizing the need to minimize annual SZA variation when defining CSA.

The S-CSA condition effectively addresses the limitations of other geometry conditions. The selected solar geometry is within the range of observation geometry, meaning that it does not induce angular extrapolation uncertainties. The S-CSA condition also avoids hot-spots; thus, EVI2 time-series does not exhibit spikes (figure S4(c)). Furthermore, unlike the pixel-by-pixel T-CSA condition, which causes large annual SZA variation and spatial discontinuities, the S-CSA condition applies a uniform scattering angle across Southeast Asia, mitigating solar angle effects and ensuring spatial consistency. Consequently, EVI2 under the S-CSA condition showed seasonal variation that was least affected by the BRDF effects and higher correlations with tower-based GPP at almost all sites. Moreover, like MODIS NBAR, the S-CSA condition is not subject to regional bias or longitude dependence, enabling consistent pixel-to-pixel comparisons across Southeast Asia (figures 4(d), (e) and S5).

To test whether the results were sensitive to the specific choice of scattering angle in S-CSA, we also applied the S-CSA method using 135° and 145° (figure S6). The results were nearly identical to those at 140°, confirming that the S-CSA approach is robust to small variations in the selected scattering angle.

Hot-spot effects—enhanced canopy reflectance resulting from shadow hiding when the sensor and Sun are nearly aligned in the backscattering direction—differ from general BRDF distortions, which stem from broader anisotropic reflectance under changing illumination and viewing geometries. GEO satellites, due to their consistent revisit geometries, are particularly prone to repeated nearbackscatter observations, making hot-spot artifacts more common and temporally disruptive (Yang et al 2025). By enforcing a S-CSA, the S-CSA approach avoids near-backscattering conditions and thus effectively reduces hot-spot noise in high-frequency vegetation monitoring.

The S-CSA condition has the potential to greatly improve vegetation monitoring in tropical regions. Based on the spatial relationship between the study area (90° E–165° E, 12° S–23° N) and the Himawari AHI (140.7° E, 0° S), the S-CSA condition was shown to be applicable within a maximum range of $\pm 23^{\circ}$ in latitude and $\pm 50^{\circ}$ in longitude from the subsatellite point. This range can be extended by integrating multiple GEO satellites to cover nearly the entire tropical region. In principle, the S-CSA method is not limited to Himawari-8/9 but can also be applied to other geostationary platforms, such as GK-2A, GOES-16, and FY-4A, since it depends solely on the relative geometry among the satellite, the surface, and the Sun. This implies that the approach could be extended to the entire tropical regions beyond Southeast Asia, including the Amazon Basin and Central Africa. Such expanded coverage enables

hyper-temporal vegetation monitoring across tropics and mitigates the impact of spatial variation in viewing geometry among pixels, a key challenge in GEO satellite observations. Therefore, the S-CSA condition offers promising opportunities for more detailed and extensive vegetation dynamics analysis, in particular over tropical regions worldwide.

Although flux-based validation in this study was restricted to evergreen and deciduous broadleaf forest sites, we also applied the method to cropland sites in Vietnam and the Philippines, where flux observation data were not available (figure S7). The results indicated that S-CSA consistently provided the most stable and coherent vegetation index signals compared with other geometry definitions. This suggests that the benefit of enforcing spatially uniform scattering geometry is not limited to forests but can also extend to heterogeneous landscapes such as croplands. Future work should further validate these results with flux observations from additional land-cover types.

This study evaluated the S-CSA method mainly using flux datasets from 2018–2019, which, although consistent and complete, cover only a short period and do not capture full interannual variability. Extreme climate conditions, such as El Niño, were therefore not explicitly tested. However, since the S-CSA method depends only on the relative geometry among the satellite, the surface, and the Sun, it is in principle applicable to any year. This implies that vegetation responses to interannual variability should also be detectable. Future work will extend the analysis to multi-year datasets, including extreme years, to further confirm the robustness of the method.

5. Conclusion

This study introduced the S-CSA condition as the most effective sun-target-sensor geometry for the Himawari AHI to ensure uniform observation geometry across Southeast Asia. Compared to other geometry conditions, the S-CSA condition effectively mitigated BRDF-induced artifacts and noise, while maintaining spatial consistency across the region. Consequently, EVI2 derived under the S-CSA condition showed stronger correlations with tower-based GPP and more accurately captured seasonal vegetation activity. These findings underscore the importance of applying uniform sun-target-sensor geometry for consistent vegetation monitoring using GEO satellites.

The S-CSA approach overcomes a key limitation of geostationary satellites, namely the spatial variation in viewing geometry across pixels, by providing spatially homogeneous relative conditions. This enables spatially consistent and high-frequency vegetation monitoring across large regions, including Southeast Asia and tropical rainforest areas.

Beyond methodological advances, the approach also has potential applications in carbon monitoring frameworks, such as REDD+ initiatives and tropical forest management programs, where robust and consistent monitoring of vegetation dynamics is essential.

Data availability statement

Himawari surface reflectance products are publicly available via: ftp://modis.cr.chiba-u.ac.jp/ichii/SEND_NEW/H8AHI_SR. The flux data can be downloaded from the JapanFlux2024 dataset (https://ads.nipr.ac.jp/japan-flux2024/) for the LHP and MMP sites, the AsiaFlux database (https://db.cger.nies.go.jp/asiafluxdb/) for the MKL and SKR sites, and Zenodo (https://zenodo.org/records/4835696) for the DTP and ITP sites.

Acknowledgment

This work was supported by research grants from the Japan Society for the Promotion of Science (JSPS; Grant Numbers KAKENHI JP22H05004, JP20K20487, and JP23KJ0304); the JSPS Core-to-Core Program (Grant Number JPJSCCA20220008); JST SPRING (Grant Number JPMJSP2109); the Virtual Laboratory (VL) project supported by the Ministry of Education, Culture, Sports, Science and Technology (MEXT), Japan; and the IAAR Research Support Program of Chiba University. Asia Pacific Resources International Ltd (APRIL) and Riau Ecosystem Restoration (RER) supported the establishment and operation of the eddy-covariance towers at the ITP and DTP sites and the associated data collection.

Author contributions

Misaki Hase D 0009-0000-7581-9959

Conceptualization (equal), Formal analysis (lead), Methodology (lead), Software (lead), Visualization (lead), Writing – original draft (lead),

Writing – review & editing (lead)

Writing – review & editing (lead)

Kazuhito Ichii © 0000-0002-8696-8084 Conceptualization (equal), Funding

acquisition (lead), Project administration (lead), Validation (lead), Writing – review & editing (lead)

Yuhei Yamamoto © 0000-0001-8982-9218 Validation (supporting), Writing – review & editing (supporting)

Wei Li 📵 0009-0002-6217-4877

Data curation (equal), Writing – review & editing (supporting)

Beichen Zhang © 0000-0001-9378-0250 Data curation (equal), Writing – review & editing (supporting) Wei Yang © 0000-0002-4597-877X Validation (supporting), Writing – review & editing (supporting)

Tomo'omi Kumagai © 0000-0001-8331-271X Data curation (lead), Investigation (lead), Writing – review & editing (supporting)

Yoshiaki Hata D 0000-0001-7703-0863

Data curation (lead), Investigation (lead), Writing – review & editing (supporting)

Naoya Takamura D 0000-0002-1925-7784

Data curation (lead), Investigation (lead), Writing – review & editing (supporting)

Chandra S Deshmukh © 0000-0003-2660-4315 Data curation (lead), Investigation (lead), Writing – review & editing (supporting)

Masahito Ueyama © 0000-0002-4000-4888 Data curation (lead), Investigation (lead), Writing – review & editing (supporting)

Hiroki Yoshioka © 0000-0002-0978-8610 Data curation (supporting), Investigation (supporting), Writing – review & editing (supporting)

Tomoaki Miura © 0000-0002-0882-3568 Conceptualization (equal), Methodology (equal), Validation (supporting), Writing – review & editing (supporting)

References

Bastos A et al 2020 Sources of uncertainty in regional and global terrestrial CO₂ exchange estimates Glob. Biogeochem. Cycles 34 e2019GB006393

Buchhorn M, Lesiv M, Tsendbazar N-E, Herold M, Bertels L and Smets B 2020 Copernicus global land cover layers—collection 2 *Remote Sens.* 12 1044

Camacho-de Coca F, Bréon F M, Leroy M and Garcia-Haro F J 2004 Airborne measurement of hot spot reflectance signatures *Remote Sens. Environ.* **90** 63–75

Deshmukh C S *et al* 2021 Conservation slows down emission increase from a tropical peatland in Indonesia *Nat. Geosci.* **14** 484–90

Fensholt R, Sandholt I, Stisen S and Tucker C 2006 Analysing NDVI for the African continent using the geostationary meteosat second generation SEVIRI sensor *Remote Sens. Environ.* **101** 212–29

Gao F, Schaaf C B, Strahler A H and Lucht W 2001 Using a multikernel least-variance approach to retrieve and evaluate albedo from limited bidirectional measurements *Remote Sens. Environ.* 76 57–66

Gao S, Zhang X, Zhang H K, Shen Y, Roy D P, Wang W and Schaaf C 2024 A new constant scattering angle solar geometry definition for normalization of GOES-R ABI reflectance times series to support land surface phenology studies Remote Sens. Environ. 315 114407

Hally B, Wallace L, Reinke K, Jones S and Skidmore A 2019 Advances in active fire detection using a multi-temporal method for next-generation geostationary satellite data *Int. J. Digit. Earth* 12 1030–45

Hashimoto H, Wang W, Dungan J L, Li S, Michaelis A R, Takenaka H, Higuchi A, Myneni R B and Nemani R R 2021 New generation geostationary satellite observations support

- seasonality in greenness of the Amazon evergreen forests Nat. Commun. 12 684
- Huete A R, Restrepo-Coupe N, Ratana P, Didan K, Saleska S R, Ichii K, Panuthai S and Gamo M 2008 Multiple site tower flux and remote sensing comparisons of tropical forest dynamics in Monsoon Asia Agric. For. Meteorol. 148 748–60
- Huete A, Didan K, Miura T, Rodriguez E P, Gao X and Ferreira L G 2002 Overview of the radiometric and biophysical performance of the MODIS vegetation indices *Remote Sens. Environ.* 83 195–213
- Ichii K et al 2017 New data-driven estimation of terrestrial CO₂ fluxes in Asia using a standardized database of eddy covariance measurements, remote sensing data, and support vector regression J. Geophys. Res. Biogeosci. 122 767–95
- Iqbal M 1983 An Introduction to Solar Radiation (Academic Press) (https://doi.org/10.1016/B978-0-12-373750-2.50016-1)
- Ishida A *et al* 2010 Seasonal variations of gas exchange and water relations in deciduous and evergreen trees in monsoonal dry forests of Thailand *Tree Physiol.* **30** 935–45
- Jeong S et al 2023 Tracking diurnal to seasonal variations of gross primary productivity using a geostationary satellite, GK-2A advanced meteorological imager Remote Sens. Environ. 284 113365
- Jiang Z, Huete A R, Didan K and Miura T 2008 Development of a two-band enhanced vegetation index without a blue band Remote Sens. Environ. 112 3833–45
- Khan A M, Stoy P C, Joiner J, Baldocchi D, Verfaillie J, Chen M and Otkin J A 2022 The diurnal dynamics of gross primary productivity using observations from the advanced baseline imager on the geostationary operational environmental satellite-R series at an oak savanna ecosystem J. Geophys. Res. Biogeosci. 127 e2021JG006701
- Kondo M et al 2018 Land use change and El Niño-Southern oscillation drive decadal carbon balance shifts in Southeast Asia Nat. Commun. 9 1154
- Li W *et al* 2025 Estimation and evaluation of land surface reflectance from a next-generation geostationary meteorologicalsSatellite, Himawari-8/9 AHI *J. Meteorol. Soc. Jpn.* 103 87–109
- Li X, Ryu Y, Xiao J, Dechant B, Liu J, Li B, Jeong S and Gentine P 2023 New-generation geostationary satellite reveals widespread midday depression in dryland photosynthesis during 2020 western U.S. heatwave *Sci. Adv.* **9** eadi0775
- Li X and Strahler A H 1992 Geometric-optical bidirectional reflectance modeling of the discrete crown vegetation canopy: effect of crown shape and mutual shadowing *IEEE Trans. Geosci. Remote Sens.* 30 276–92
- Li Z, Roy D P and Zhang H K 2021 The incidence and magnitude of the hot-spot bidirectional reflectance distribution function (BRDF) signature in GOES-16 advanced baseline imager (ABI) 10 and 15 minute reflectance over north America Remote Sens. Environ. 265 112638
- Liu Y *et al* 2017 Evaluation of the VIIRS BRDF, Albedo and NBAR products suite and an assessment of continuity with the long term MODIS record *Remote Sens. Environ.* **201** 256–74
- Lucht W, Schaaf C B and Strahler A H 2000 An algorithm for the retrieval of albedo from space using semiempirical BRDF models *IEEE Trans. Geosci. Remote Sens.* **38** 977–98
- Morton D C, Nagol J, Carabajal C C, Rosette J, Palace M, Cook B D, Vermote E F, Harding D J and North P R J 2014 Amazon forests maintain consistent canopy structure and greenness during the dry season *Nature* 506 221–4
- Nagai S, Ishii R, Suhaili A B, Kobayashi H, Matsuoka M, Ichie T, Motohka T, Kendawang J J and Suzuki R 2014 Usability of noise-free daily satellite-observed green–red vegetation index values for monitoring ecosystem changes in Borneo Int. J. Remote Sens. 35 7910–26
- Pan Y *et al* 2024 The enduring world forest carbon sink *Nature*
- Reichstein M et al 2005 On the separation of net ecosystem exchange into assimilation and ecosystem respiration:

- review and improved algorithm *Glob. Change Biol.* 11 1424–39
- Roy D P, Zhang H K, Ju J, Gomez-Dans J L, Lewis P E, Schaaf C B, Sun Q, Li J, Huang H and Kovalskyy V 2016 A general method to normalize Landsat reflectance data to nadir BRDF adjusted reflectance *Remote Sens. Environ*. 176 255–71
- Satriawan T W, Luo X, Tian J, Ichii K, Juneng L and Kondo M 2024 Strong green-up of tropical Asia during the 2015/16 El Niño *Geophys. Res. Lett.* 51 e2023GL106955
- Schaaf C B *et al* 2002 First operational BRDF, albedo nadir reflectance products from MODIS *Remote Sens. Environ.* **83** 135–48
- Takamura N, Hata Y, Matsumoto K, Kume T, Ueyama M and Kumagai T 2023 El Niño-Southern oscillation forcing on carbon and water cycling in a Bornean tropical rainforest *Proc. Natl Acad. Sci. USA* 120 e2301596120
- Takenaka H, Sakashita T, Higuchi A and Nakajima T 2020 Geolocation correction for geostationary satellite observations by a phase-only correlation method using a visible channel *Remote Sens.* 12 2472
- Tian J, Luo X, Wang W, Yu L, Ng D T T, Ichii K, Zhang Y and Zhang X 2025 Seasonality of vegetation greenness in Southeast Asia unveiled by geostationary satellite observations *Remote Sens. Environ.* **319** 114648
- Ueyama M *et al* 2025 The JapanFlux2024 dataset for eddy covariance observations covering Japan and East Asia from 1990 to 2023 *Earth Sys. Sci. Data Discuss* 17 1–47
- Ueyama M, Hirata R, Mano M, Hamotani K, Harazono Y and Hirano T, Miyata A, Takagi K and Takahashi Y 2012 Influences of various calculation options on heat, water and carbon fluxes determined by open- and closed-path eddy covariance methods *Tellus B* 64 19048
- Vancutsem C, Achard F, Pekel J-F, Vieilledent G, Carboni S, Simonetti D, Gallego J, Aragão L E O C and Nasi R 2021 Long-term (1990–2019) monitoring of forest cover changes in the humid tropics *Sci. Adv.* 7 eabe1603
- Vancutsem C, Pekel J-F, Bogaert P and Defourny P 2007 Mean compositing, an alternative strategy for producing temporal syntheses. Concepts and performance assessment for SPOT VEGETATION time series *Int. J. Remote Sens.* 28 5123–41
- Vermote E F and Roy D P 2002 Land surface hot-spot observed by MODIS over Central Africa *Int. J. Remote Sens.* 23 2141–3
- Watson J E M et al 2018 The exceptional value of intact forest ecosystems Nat. Ecol. Evol. 2 599–610
- Wiggins E B *et al* 2020 High temporal resolution satellite observations of fire radiative power reveal link between fire behavior and aerosol and gas emissions *Geophys. Res. Lett.* 47 e2020GL090707
- Yamamoto Y, Ichii K, Higuchi A and Takenaka H 2020 Geolocation accuracy assessment of Himawari-8/AHI imagery for application to terrestrial monitoring *Remote* Sens. 12 1372
- Yamamoto Y, Ishikawa H, Oku Y and Hu Z 2018 An algorithm for land surface temperature retrieval using three thermal infrared bands of Himawari-8 *J. Meteorol. Soc. Jpn.* **96** 59–76
- Yang W, Qiao Z, Li W, Ma X and Ichii K 2025 An enhanced RPV model to better capture hotspot signatures in vegetation canopy reflectance observed by the geostationary meteorological satellite Himawari-8 Sci. Remote Sens. 11 100222
- Yoshifuji N, Kumagai T, Tanaka K, Tanaka N, Komatsu H, Suzuki M and Tantasirin C 2006 Inter-annual variation in growing season length of a tropical seasonal forest in northern Thailand *For. Ecol. Manage.* **229** 333–9
- Zhang B, Ichii K, Li W, Yamamoto Y, Yang W, Sharma R C, Yoshioka H, Obata K, Matsuoka M and Miura T 2025 Evaluation of Himawari-8/AHI land surface reflectance at mid-latitudes using LEO sensors with off-nadir observation *Remote Sens. Environ.* 316 114491
- Zhang H K, Roy D P and Kovalskyy V 2016a Optimal solar geometry definition for global long-term Landsat

time-series bidirectional reflectance normalization *IEEE Trans. Geosci. Remote Sens.* **54** 1410–8

Zhang X *et al* 2021 Evaluation of BRDF information retrieved from time-series multiangle data of the Himawari-8 AHI *Remote Sens.* 14 139

Zhang X, Shen Y, Gao S, Wang W and Schaaf C 2022 Diverse responses of multiple satellite-derived vegetation greenup

onsets to dry periods in the Amazon *Geophys. Res. Lett.* **49** e2022GL098662

Zhang Y, Zhu Z, Liu Z, Zeng Z, Ciais P, Huang M, Liu Y and Piao S 2016b Seasonal and interannual changes in vegetation activity of tropical forests in Southeast Asia *Agric. For. Meteorol.*224 1–10